Journal of
Materials Chemistry A

ROYAL SOCIETY
OF CHEMISTRY

PAPER

View Article Online
View Journal | View Issue

Cite this: *J. Mater. Chem. A*, 2023, **11**, 9989

Visible-light-driven and selective methane conversion to oxygenates with air on a halide-perovskite-based photocatalyst under mild conditions†

Guang-Xing Dong,[a] Meng-Ran Zhang,[a] Ke Su,[a] Zhao-Lei Liu,[a] Min Zhang *[ab] and Tong-Bu Lu *[a]

Received 7th March 2023
Accepted 13th April 2023

DOI: 10.1039/d3ta01405c

rsc.li/materials-a

Activation and catalytic transformation of C–H bonds under mild conditions has long been a great challenge for the chemical industry. Herein, we report a halide-perovskite-based photocatalyst composed of manganese-doped $CsPbBr_3$ decorated on $BiVO_4$ for the efficient and selective transformation of nonpolar CH_4 to oxygenates using air as an oxidant. At room temperature and atmospheric pressure, the yield and selectivity of oxygen-containing hydrocarbons (CH_3OH and HCHO) from photocatalytic CH_4 oxidation are as high as 533.5 μmol g^{-1} h^{-1} and 94.8%, respectively. Moreover, transient intermediate capture and isotope labeling experiments demonstrate that the oxygen sources of products for this heterojunction are mainly from O_2, which contrasts with that from water in pristine $BiVO_4$, owing to the difference in the pathway of O_2 reduction induced by the increased thermodynamic driving force. This work provides an effective strategy for the design and development of a cost-effective catalyst system for CH_4 conversion in a mild manner.

1 Introduction

Abundant and low-cost methane (CH_4) is currently a high-quality fossil fuel, but it is also an important greenhouse gas,[1,2] and its exothermic combustion releases large amounts of CO_2. Catalytic transformation of CH_4 into a variety of high-value-added chemicals is a win–win strategy for the effective utilization of CH_4 and the suppression of carbon emissions into the atmosphere.[3,4] However, the conversion of inert CH_4 is particularly difficult, owing to its small polarizability of 2.84×10^{-40} C^2 m^2 J^{-1} and high C–H bond energy (413 kJ mol^{-1}).[5,6] At present, the mature route of methane conversion in industry is based on the thermocatalysis technology, which requires harsh conditions with huge energy consumption such as high temperature or high pressure.[7–9] Therefore, it is highly desirable to explore alternative approaches to achieve the conversion of CH_4 under mild conditions. In this regard, photocatalytic CH_4 oxidation is considered to be a promising strategy to achieve the cost-effective utilization of CH_4,[10–13] by employing inexhaustible and clean solar energy to generate hot electron–hole pairs over catalysts to directly or indirectly activate the C–H bonds of CH_4, which has attracted ever-increasing attention in recent years.

Hitherto, numerous photocatalysts, such as TiO_2,[14,15] ZnO,[16–18] CeO_2,[19,20] $BiVO_4$ (ref. [21]), g-C_3N_4 (refs. [22] and 23) *etc.*, have been demonstrated to be capable of oxidizing CH_4 into high-value-added chemicals (CH_3OH, HCHO, HCOOH *etc.*). The performance of CH_4 photooxidation has achieved encouraging progress recently, by adopting various strategies such as doping,[14,24] heterojunction engineering,[25,26] and loading metal nanoparticles[17] to create active centers, enhance light-harvesting, and promote the separation of photogenerated carriers. Nevertheless, the efficiency of CH_4 photooxidation is still far below the requirements of industrial production, owing to the short lifetime of photogenerated carriers and the dilemma resulting from the trade-off between the broad-spectrum light-harvesting ability (smaller bandgap is desired) and strong redox potential (larger bandgap is desired).[5] To achieve efficient photocatalysis of CH_4 conversion, most of the reported photocatalytic systems still need to be assisted by a certain amount of heat or high pressure,[4] and many photocatalysts with high yield and high selectivity require the assistance of additional expensive oxidants such as H_2O_2, $FeCl_3$, NO, *etc.*[4,27] In addition, the overoxidation of CH_4 always occurs easily due to the thermodynamically unstable properties of oxidation products including CH_3OH, HCHO and HCOOH, resulting in an

---

[a] *MOE International Joint Laboratory of Materials Microstructure, Institute for New Energy Materials and Low Carbon Technologies, School of Materials Science and Engineering, Tianjin University of Technology, Tianjin 300384, China. E-mail: zm2016@email.tjut.edu.cn; lutongbu@tjut.edu.cn*

[b] *Tianjin Key Laboratory of Organic Solar Cells and Photochemical Conversion, School of Chemistry and Chemical Engineering, Tianjin University of Technology, Tianjin 300384, China*

† Electronic supplementary information (ESI) available. See DOI: **https://doi.org/10.1039/d3ta01405c**

inferior selectivity of high-value-added products.[12] Consequently, it is highly anticipated to explore photocatalysts for highly efficient and selective conversion of CH_4 under mild conditions without adding costly oxidants, which is still a huge challenge and called for valid strategies toward high-performance.

Herein, we elaborately design and construct a Z-scheme heterojunction composed of manganese-doped halide perovskite $CsPbBr_3$ and bismuth vanadate ($BiVO_4$) through a facile *in situ* growth strategy and employ it as a photocatalyst to convert methane to oxygenates with air as an oxidant at room temperature and atmospheric pressure. Of note, halide perovskites possess excellent photophysical properties such as high extinction coefficients, low exciton binding energy and long electron–hole diffusion lengths,[28] which are desirable for the effective utilization of solar photons. In addition, compared with pristine $BiVO_4$, decorating $CsPbBr_3$ nanocrystals on $BiVO_4$ with Z-scheme mode can not only significantly ameliorate the separation of photogenerated carriers, but also enhance the reduction capacity of photocatalysts,[29,30] both of which facilitate the over-all photocatalytic reaction of CH_4 conversion. As expected, the as-prepared $Mn@CsPbBr_3/BiVO_4$ photocatalyst exhibits excellent performance for CH_4 conversion to CH_3OH and HCHO with a total yield of 533.5 μmol g^{-1} h^{-1}, which is 8.8 times higher than that of pristine $BiVO_4$. In addition, the product selectivity of oxygenates is as high as 94.8% in a well-designed circulating flow reactor. Moreover, both the reduction and oxidation reaction mechanisms of pristine $BiVO_4$ and the $Mn@CsPbBr_3/BiVO_4$ heterojunction are scrutinized through joint isotope labeling, intermediate detection and controlled experiments.

2 Experimental

2.1 Materials

Bismuth nitrate pentahydrate ($Bi(NO_3)_3 \cdot 5H_2O$, 98%), sodium metavanadate ($NaVO_3$, 99.9%), and acetic acid ($C_2H_4O_2$, 99.5%) were obtained from Adamas-Beta. Oleic acid (OA, 90%), oleylamine (OLA, 80%) and 1-octadecene (ODE, 90%) were purchased from Aladdin. Lead(II) bromide ($PbBr_2$, 99.99%) was obtained from Xi'an Polymer Light Technology Corp. Cesium carbonate (Cs_2CO_3, 99.7%) was obtained from J&K Scientific. Manganese(II) bromide anhydrous ($MnBr_2$, 99%), coumarin ($C_9H_6O_2$, 99%), 5,5-dimethyl-1-pyrroline-*N*-oxide (DMPO), and acetylacetone ($C_5H_8O_2$, 99%) were purchased from Tokyo Chemical Industry (TCI). $H_2{}^{18}O$, $^{18}O_2$, and $^{13}CH_4$ were obtained from Wuhan Isotope Technology.

2.2 Preparation of $BiVO_4$

$Bi(NO_3)_3 \cdot 5H_2O$ (1 M) and $NaVO_3$ (0.1 M) were dissolved in acetic acid and deionized water with the assistance of ultrasonication, respectively, and then mixed with a molar ratio of Bi to V of 1 : 1 to form a yellow suspension, which was sealed and stirred for 1 h. Thereafter, the mixture was transferred to a stainless-steel autoclave with a Teflon-liner, which was heated to 150 °C with a ramp rate of 10 °C min^{-1} and kept for 20 h. Finally, the precipitate was washed with deionized water, dried overnight, and calcined at 300 °C for 4 h to generate the $BiVO_4$ sample.

2.3 Preparation of $CsPbBr_3$ and $Mn@CsPbBr_3$ seed clusters

$CsPbBr_3$ and $Mn@CsPbBr_3$ seed clusters were synthesized according to a previously reported approach[31] with slight modification. Briefly, 652 mg of Cs_2CO_3 and 2.5 mL of OA were added into a three-necked flask with 17.5 mL of ODE. The mixture was degassed at 120 °C for 1 h under an Ar flow and then heated to 150 °C and kept for 30 min until the entire precursor dissolved to generate a cesium precursor (a pale yellowish transparent solution). 734 mg of $PbBr_2$, 6 mL of OA, and 6 mL of OLA were added into a three-necked flask pre-filled with 32 mL of ODE. After degassing in a stream of Ar at 120 °C for 1 h to completely dissolve $PbBr_2$, the reaction mixture was allowed to cool to room temperature naturally. Then 2.2 mL of preheated cesium precursor (80 °C) was injected into the $PbBr_2$ solution followed by vigorous stirring for 25 min, and the mixture turned cloudy, indicating the formation of seed clusters. The as-synthesized seed clusters were precipitated out of the crude mixture by centrifugation at 6000 rpm for 10 min. The obtained precipitate was redispersed in 5 mL ODE. The $CsPbBr_3$ seed solution needs to be kept cold in a refrigerator before use, as the seed clusters are very unstable. The synthesis process of $Mn@CsPbBr_3$ seed clusters is similar to that of its $CsPbBr_3$ counterpart, except that 8 mg, 16 mg, and 32 mg of $MnBr_2$ were added into the $PbBr_2$ solution, and the obtained samples were denoted as $Mn_{0.12\%}@CsPbBr_3$, $Mn_{0.27\%}@CsPbBr_3$, $Mn_{0.42\%}@CsPbBr_3$ seed clusters, respectively.

2.4 Preparation of $CsPbBr_3/BiVO_4$ and $Mn@CsPbBr_3/BiVO_4$

$CsPbBr_3/BiVO_4$ and $Mn@CsPbBr_3/BiVO_4$ were prepared through an *in situ* growth method. ODE (15 mL) was added to a 50 mL three-neck round-bottom flask, degassed for 1 h under a stream of Ar at 120 °C, and then heated to 180 °C. Then, 1 mL of ODE dispersed with 50 mg $BiVO_4$ and 0.5 mL of the as-prepared $CsPbBr_3$ seed cluster solution were rapidly injected into the hot ODE solvent. After 30 s, the reaction mixture was cooled with an ice-water bath. $CsPbBr_3{}^{0.5}/BiVO_4$ can be separated from the crude mixture by centrifugation at 6000 rpm for 10 min. By the same method, $CsPbBr_3{}^{1}/BiVO_4$, $CsPbBr_3{}^{1.5}/BiVO_4$ and $CsPbBr_3{}^{2}/BiVO_4$ can be obtained by changing the added amounts of $CsPbBr_3$ seed cluster solution to 1 mL, 1.5 mL, and 2 mL, respectively. The preparation processes of $Mn@CsPbBr_3/BiVO_4$ were the same as those of $CsPbBr_3{}^{1.5}/BiVO_4$, except that $CsPbBr_3$ seed clusters were replaced by $Mn_{0.12\%}@CsPbBr_3$, $Mn_{0.27\%}@CsPbBr_3$, $Mn_{0.42\%}@CsPbBr_3$ seed clusters, respectively.

2.5 Performance evaluation of photocatalytic CH_4 conversion

The photocatalytic measurements of CH_4 oxidation with air (O_2) were carried out in a circulating gas flow system. First, 10 mg of the photocatalyst was dispersed in 5 mL of *n*-hexane and then spread evenly on a hydrophilic polyethersulfone membrane with a pore size of 0.44 μm and diameter of 25 mm. After gentle annealing/drying at 50 °C and weighing, it was placed into a reactor. After filling the reactor with a 10 : 1 mixture of CH_4 (99.999%) and air through the photoreactor in the dark for 1 h, the reaction system was sealed, and the mixed gas was circulated in the photoreactor at a flow rate of 20 mL min^{-1} under the action of a peristaltic pump. The reaction system was irradiated with a 300 W Xe lamp (400 nm filter) at room temperature for 3 h, and the light intensity was adjusted to 100 mW cm^{-2} by NREL-calibrated Si solar cell calibration. In addition, in order to carry out the free radical quench experiment smoothly, 10 mg photocatalyst was dispersed in 5 mL acetonitrile with different quenchers and placed in a photoreactor irradiated under similar conditions for 4 h.

3 Results and discussion

3.1 Synthesis and structure characterization

The $BiVO_4$ substrate was synthesized according to the hydrothermal method as reported in a previous publication,[32] and the details were described in the Experimental section. The scanning electron microscope (SEM) measurements revealed that the morphology of as-prepared $BiVO_4$ is a dumbbell-shaped microsphere with a rough surface (Fig. 1a and S1†). $CsPbBr_3$ nanocrystals were *in situ* grown on the surface of the $BiVO_4$ substrate to generate a $CsPbBr_3/BiVO_4$ composite, and the detailed preparation processes are described in the Experimental section. Under the same conditions, $BiVO_4$ decorated with Mn-doped $CsPbBr_3$ nanocrystals (denoted as $Mn@CsPbBr_3/BiVO_4$) can be obtained by adding a certain amount of $MnBr_2$ in the $CsPbBr_3$ precursor solution. In contrast with pristine $BiVO_4$, many dispersed nanocrystals with a size of 10∼30 nm can be clearly observed on the surface of $BiVO_4$ in $CsPbBr_3/BiVO_4$ (Fig. 1b) and $Mn@CsPbBr_3/BiVO_4$ (Fig. S2†) composites, implying the successful deposition of $CsPbBr_3$ and Mn-doped $CsPbBr_3$ on the surface of the $BiVO_4$ substrate. Energy-dispersive X-ray spectroscopy (EDS) mapping measurements demonstrated that Cs, Pb, and Br elements are evenly distributed on the surface of $BiVO_4$ (Fig. 1c–h) in the $CsPbBr_3/BiVO_4$ composite, suggesting the homogeneous dispersion of $CsPbBr_3$ nanocrystals on the surface of the $BiVO_4$ substrate. The elemental mapping images of $Mn@CsPbBr_3/BiVO_4$ (Fig. S3 and S4†) also show that the surface of the $BiVO_4$ matrix is decorated with highly dispersed Mn-doped $CsPbBr_3$ nanocrystals. For comparison, pristine $CsPbBr_3$ nanocrystals (Fig. S5†) were also prepared without adding the $BiVO_4$ substrate, while keeping other parameters unvaried.

The high-resolution transmission electron microscopy (HRTEM) image of the $CsPbBr_3/BiVO_4$ composite reveals that the as-prepared $BiVO_4$ is indexed to the scheelite monoclinic phase with a clear lattice spacing of 3.08 Å as shown in Fig. 1i, which can be assigned to the (121) lattice plane of $BiVO_4$. Meanwhile, a distinct lattice spacing of 2.06 Å can also be identified in the HRTEM image of $CsPbBr_3/BiVO_4$, corresponding to the (220) crystal plane of cubic phase $CsPbBr_3$. X-

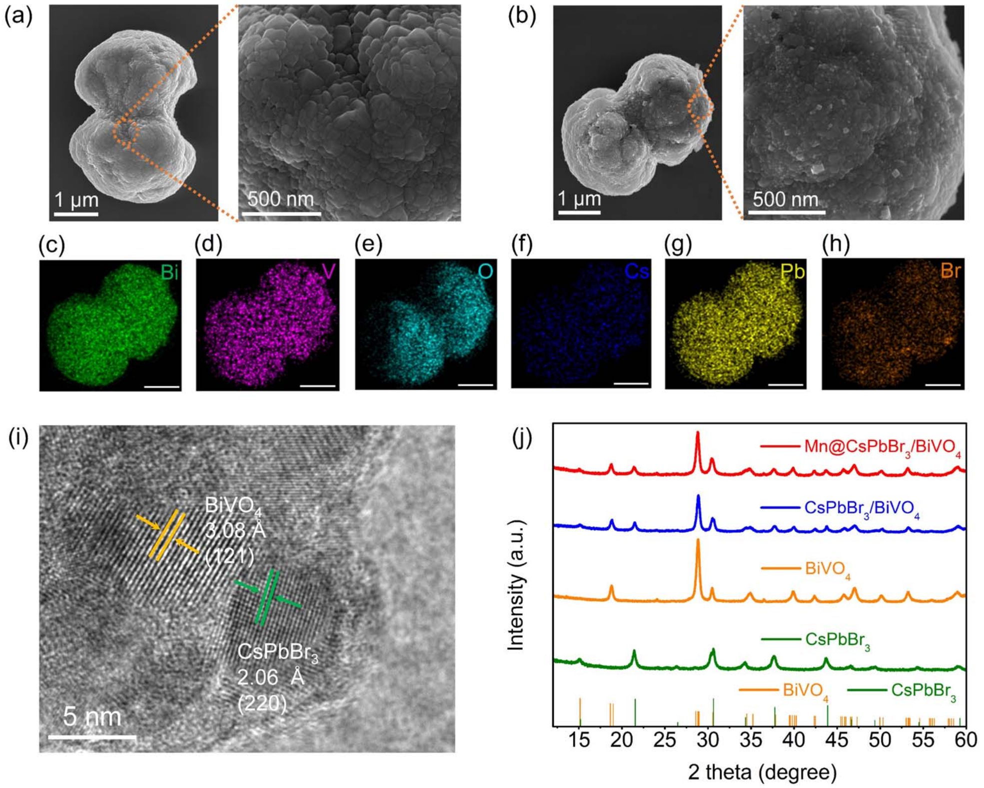

Fig. 1 SEM images of (a) $BiVO_4$ and (b) $CsPbBr_3/BiVO_4$. (c–h) Elemental mapping images of $CsPbBr_3/BiVO_4$ with a scale bar of 1 μm. (i) High-resolution TEM image of $CsPbBr_3/BiVO_4$ showing the lattice spacings. (j) XRD patterns of $BiVO_4$, $CsPbBr_3$, $CsPbBr_3/BiVO_4$ and $Mn@CsPbBr_3/BiVO_4$.

ray diffraction (XRD) measurements can further confirm the composition of the $CsPbBr_3/BiVO_4$ composite. As presented in Fig. 1j, the powder XRD pattern of $BiVO_4$ exhibits typical diffraction peaks for scheelite monoclinic $BiVO_4$, matching well with the standard pattern of JCPDS:14-0688. In addition, the XRD pattern of pristine $CsPbBr_3$ agrees well with that of a cubic crystal structure (JCPDS:54-0752), displaying typical diffraction peaks at a 2θ of 15.2°, 21.5°, 37.7° and 43.9°, which can be attributed to the (100), (110), (211), and (220) planes of cubic phase $CsPbBr_3$. In the XRD pattern of $CsPbBr_3/BiVO_4$, both the characteristic diffraction peaks of monoclinic $BiVO_4$ and cubic $CsPbBr_3$ can be clearly identified, again confirming that the $CsPbBr_3$ nanocrystals were successfully loaded on the $BiVO_4$ substrate. Moreover, the replacement of $CsPbBr_3$ with Mn-doped $CsPbBr_3$ nanocrystals does not bring forth an obvious change in XRD signals of composites (Fig. S6†), revealing that a small amount of metal cation doping has no significant impact on the structure of $CsPbBr_3$.

High resolution X-ray photoelectron spectroscopy (XPS) measurements were further performed to investigate the interaction between $CsPbBr_3$ and $BiVO_4$ in the $CsPbBr_3/BiVO_4$ composite. As shown in Fig. S7a–d,† compared with Br 3d and Pb 4f in original $CsPbBr_3$ nanocrystals, the binding energies of the corresponding elements in the $CsPbBr_3/BiVO_4$ composite display a perceptible positive shift (0.15–0.25 eV), while the V 2p and Bi 4f peaks in the $CsPbBr_3/BiVO_4$ composite exhibit an appreciable shift to the low-energy region by 0.25–0.30 eV in comparison with those in individual $BiVO_4$. These obvious changes in the binding energies of the aforementioned elements imply that there is a strong electron coupling between $CsPbBr_3$ and $BiVO_4$ in the $CsPbBr_3/BiVO_4$ composite, which should facilitate charge transfer at the interface of $CsPbBr_3/BiVO_4$. In general, the decrease and increase in binding energies reflect the accumulation and consumption of electrons around the nucleus, respectively. Thereby, the free electrons on the surface of $CsPbBr_3$ are transferred to $BiVO_4$ when $CsPbBr_3$ nanocrystals are decorated on the surface of the $BiVO_4$ substrate, bringing forth the formation of a built-in electric field pointing from $CsPbBr_3$ to $BiVO_4$.

3.2 Direct Z-scheme mechanism of the $CsPbBr_3/BiVO_4$ heterojunction

The built-in electric field can drive the transfer and separation of photogenerated electrons and holes through the Coulomb force, due to the opposite-electricity of photogenerated electrons and holes, which plays an important role in enhancing photocatalytic activity.[33,34] To clarify the physical origin of the built-in electric field and the pathway of photogenerated carrier transfer at the interface of $CsPbBr_3/BiVO_4$, we first evaluated the energy band structures of $BiVO_4$ and $CsPbBr_3$ by UV-visible diffuse reflectance spectroscopy (UV-Vis DRS) and ultraviolet photoelectron spectroscopy (UPS) measurements. As depicted in Fig. 2a and b, both $BiVO_4$ and $CsPbBr_3$ show good response in the visible light region with absorption edges of approximately 534 and 550 nm, respectively. Based on the corresponding Tauc plots (insets of Fig. 2a and b), we can deduce the bandgaps of $BiVO_4$ and $CsPbBr_3$ to be 2.24 and 2.30 eV, respectively, which are in accordance with previous reports on $BiVO_4$ (ref. [35]) and $CsPbBr_3$ (ref. [36]) According to the UPS spectra as presented in Fig. 2c, the valence band (VB) edge potentials (E_{VB}) of $BiVO_4$ and $CsPbBr_3$ can be determined to be 2.74 and 1.68 V *vs.* the standard hydrogen electrode (SHE), respectively. Subsequently, the conduction band (CB) edge potentials (E_{CB}) can be calculated from the difference between the values of E_G and E_{VB}, being 0.50 and −0.62 V (*vs.* SHE) for $BiVO_4$ and $CsPbBr_3$, respectively,

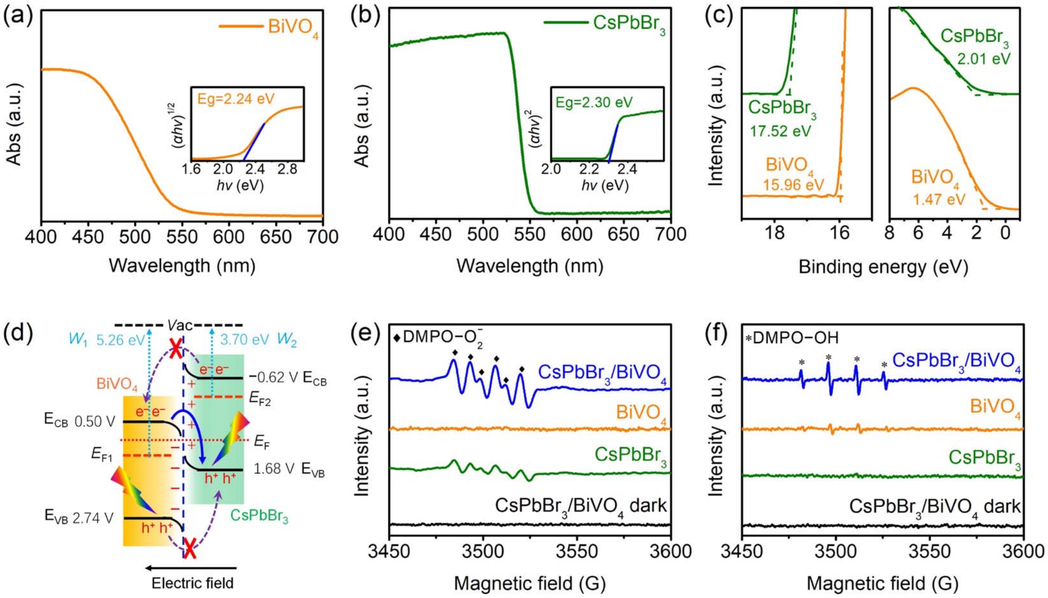

Fig. 2 UV-Vis DRS and Tauc plots (inset) of (a) $BiVO_4$ and (b) $CsPbBr_3$. (c) The UPS spectra of $BiVO_4$ and $CsPbBr_3$. (d) Energy band structures of $CsPbBr_3$ and $BiVO_4$, and the schematic illustration of the charge-transfer mechanism of the direct Z-scheme in $CsPbBr_3/BiVO_4$. EPR spectra of (e) DMPO–O_2^- and (f) DMPO–OH for $BiVO_4$, $CsPbBr_3$ and $CsPbBr_3/BiVO_4$.

which are close to the flat-band potentials of $BiVO_4$ (0.45 V) and $CsPbBr_3$ (−0.72 V) derived from their Mott–Schottky plots (Fig. S8a and b†). Apparently, there is a staggered energy band alignment between $BiVO_4$ and $CsPbBr_3$ in the $CsPbBr_3/BiVO_4$ heterojunction as visualized in Fig. S9.†

It is well known that the built-in electric field at the interface of a heterojunction is caused by the difference in Fermi levels (E_F) of each component, which has a significant impact on the interfacial charge transfer route of typical Type II heterostructures.[29] Therefore, we further estimated the E_F positions of $BiVO_4$ and $CsPbBr_3$ according to their UPS spectra (Fig. 2c), located at −5.26 and −3.70 eV (*vs.* vacuum), respectively. In order to achieve the E_F equilibrium of the composite, the incorporation of $CsPbBr_3$ onto $BiVO_4$ will result in the migration of free electrons on the surface of $CsPbBr_3$ towards $BiVO_4$, which is consistent with the result of the aforementioned XPS analysis. The resultant interfacial built-in electric field with a direction from $CsPbBr_3$ to $BiVO_4$ and corresponding band bendings will lead to the preferential choice of a direct Z-scheme route for photogenerated carriers rather than the traditional double-charge transfer mode as illustrated in Fig. 2d. *In situ* irradiated X-ray photoelectron spectroscopy (ISI-XPS) measurements[37] were carried out to scrutinize the interfacial charge migration route of the $CsPbBr_3/BiVO_4$ heterojunction. As depicted in Fig. S10a and d,† the binding energies of Pb 4f and Br 3d in the composites show a negative shift (0.15–0.2 eV) before and after light irradiation, while the binding energies of Bi 4f and V 2p move in the opposite direction. These photoinduced shifts in binding energies of constituent elements indicate that $BiVO_4$ and $CsPbBr_3$ in $CsPbBr_3/BiVO_4$ undergo electron depletion and accumulation, respectively, confirming a direct Z-scheme charge transfer mechanism for the photogenerated carriers in the $CsPbBr_3/BiVO_4$ heterojunction.

To further verify the direct Z-scheme transfer pathway of photogenerated carriers in the $CsPbBr_3/BiVO_4$ heterojunction, free radical trapping experiments were first conducted with 5,5-dimethyl-1-pyrroline-*N*-oxide (DMPO) as a trapping agent. The redox capacities of the composite and the two individual materials were investigated by monitoring the electron paramagnetic resonance (EPR) signals of $^{\bullet}OH$ and $^{\bullet}O_2^-$ radical species.[38] As shown in Fig. 2e, $CsPbBr_3$ exhibits distinct typical signals for DMPO–O_2^- after light irradiation, while no DMPO–O_2^- signal can be detected in the case of pristine $BiVO_4$, because the photogenerated electrons in the CB of $BiVO_4$ (E_{CB} = 0.50 V) are incapable of triggering the reduction of O_2 to $^{\bullet}O_2^-$ (0.08 V *vs.* SHE). Nevertheless, there are manifestly enhanced characteristic peaks of DMPO–O_2^- for the $CsPbBr_3/BiVO_4$ heterojunction relative to sole $CsPbBr_3$ nanocrystals, which indicates that the photogenerated electrons in the CB of $CsPbBr_3$ are maintained rather than transferred to the CB of $BiVO_4$. The enhanced DMPO–O_2^- signals for the $CsPbBr_3/BiVO_4$ heterojunction should be attributed to the efficient separation of photogenerated carriers in $CsPbBr_3$ through the Z-scheme charge transfer pathway, that is, the photogenerated holes in the VB of $CsPbBr_3$ are annihilated by the photogenerated electrons in the CB of $BiVO_4$ with the assistance of the built-in electric field as illustrated in Fig. 2d. This inference can be further proved by monitoring the DMPO–OH characteristic signals of $BiVO_4$, $CsPbBr_3$ and $CsPbBr_3/BiVO_4$. As presented in Fig. 2f, there are no characteristic signals of DMPO–OH that can be detected for individual $CsPbBr_3$, due to its more negative E_{VB} (1.68 V *vs.* SHE) relative to the oxidation potential of H_2O to $^{\bullet}OH$ (2.40 V *vs.* SHE). However, the replacement of $BiVO_4$ with $CsPbBr_3/BiVO_4$ can bring forth distinctly stronger characteristic signals assigned to DMPO–OH, implying the well retained photogenerated holes in the $BiVO_4$ component of $CsPbBr_3/BiVO_4$, and the photogenerated electrons in the CB of $BiVO_4$ are transferred to recombine with the photogenerated holes in the VB of $CsPbBr_3$ to achieve efficient charge separation. Moreover, both the DMPO–OH and DMPO–O_2^- signals cannot be observed in the absence of light irradiation, demonstrating that the generation of both $^{\bullet}OH$ and $^{\bullet}O_2^-$ was driven by photogenerated carriers.

3.3 Interfacial charge transfer dynamics

Apart from the redox ability, the charge separation efficiency at the heterojunction interface also has a crucial impact on the photocatalytic performance. The interfacial transfer process of photogenerated carriers in the as-prepared heterojunctions was first estimated by the steady-state photoluminescence (PL) measurements. As presented in Fig. 3a, the pristine $BiVO_4$ sample shows very weak PL, indicating the presence of swift nonradiative processes of exciton deactivation in $BiVO_4$. It is noted that $CsPbBr_3$ nanocrystals exhibit strong yellow-green light emission with a characteristic peak at ~519 nm. Loading $CsPbBr_3$ nanocrystals on the $BiVO_4$ substrate induces a significant PL quenching, indicating that there is rapid interfacial charge transfer between $CsPbBr_3$ and $BiVO_4$ in the $CsPbBr_3/BiVO_4$ heterojunction. There is a further reduced PL intensity in the Mn@$CsPbBr_3/BiVO_4$ composite, which reveals that the introduction of Mn^{2+} ions into $CsPbBr_3$ can further ameliorate the charge separation of the heterojunction. The efficient charge separation in the $CsPbBr_3/BiVO_4$ heterojunction can be further demonstrated by monitoring the time-resolved PL

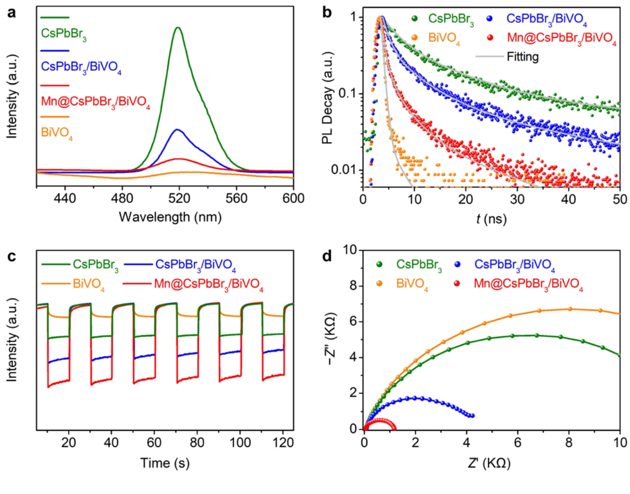

Fig. 3 (a) Steady state PL spectra and (b) time-correlated PL decay traces of $BiVO_4$, $CsPbBr_3$, $CsPbBr_3/BiVO_4$ and Mn@$CsPbBr_3/BiVO_4$. (c) *I*–*t* curves and (d) EIS Nyquist plots of $BiVO_4$, $CsPbBr_3$, $CsPbBr_3/BiVO_4$ and Mn@$CsPbBr_3/BiVO_4$.

(TRPL) decay traces as depicted in Fig. 3b, which can be well fitted with a multi-exponential function (Table S1†). $BiVO_4$ possesses a rapid PL decay with an amplitude-averaged lifetime of only 3.2 ns, implying that the photogenerated carrier lifetime of $BiVO_4$ is very short. In contrast to $BiVO_4$, $CsPbBr_3$ features dramatically sluggish PL decay with a significantly longer amplitude-averaged lifetime of 37.2 ns, demonstrating the unique properties of the long photogenerated carrier lifetime of $CsPbBr_3$. The $CsPbBr_3/BiVO_4$ heterojunction exhibits an apparent acceleration of PL decay in comparison with $CsPbBr_3$, and the amplitude-averaged lifetime of 14.2 ns for $CsPbBr_3/BiVO_4$ is significantly shorter than that of 37.2 ns for $CsPbBr_3$, indicative of rapid charge transfer at the interface of $CsPbBr_3/BiVO_4$. It is noted that the introduction of Mn^{2+} can bring forth a further accelerated PL decay with a reduced amplitude-averaged lifetime of 11.4 ns, which is attributed to the effective trapping of photogenerated electrons in $CsPbBr_3$ by doped Mn^{2+} ions.[39,40]

Transient photocurrent response and electrochemical impedance spectroscopy (EIS) measurements can further consolidate the efficient charge separation in the $CsPbBr_3/BiVO_4$ heterojunction. As compared with pristine $BiVO_4$ or $CsPbBr_3$, $CsPbBr_3/BiVO_4$ possesses a manifestly higher photocurrent density, which can be further improved by doping Mn^{2+} ions into $CsPbBr_3$ as presented in Fig. 3c. In addition, the results of EIS measurements under light irradiation (Fig. 3d) show that the semicircular radius in the Nyquist plot of the $CsPbBr_3/BiVO_4$ heterojunction is distinctly smaller than that of individual $BiVO_4$ or $CsPbBr_3$, which reveals that the decoration of $CsPbBr_3$ on $BiVO_4$ can reduce charge transfer resistance owing to the efficient charge separation. Moreover, the $Mn@CsPbBr_3/BiVO_4$ composite features an obviously smaller semicircular radius of the Nyquist plot with respect to $CsPbBr_3/BiVO_4$, further proving the favorable influence of Mn^{2+} incorporation on the interfacial charge transfer and separation.

3.4 Photocatalytic activity of CH_4 oxidation

The Z-scheme charge transfer mechanism in the $CsPbBr_3/BiVO_4$ heterojunction can ameliorate the separation of photogenerated carriers while maintaining their strong redox ability,[38] which should be beneficial for the performance promotion of photocatalytic CH_4 oxidation. In addition, decorating $CsPbBr_3$ onto $BiVO_4$ can also enhance the light-harvesting capacity of the photocatalyst (Fig. S12†), owing to the high extinction coefficient of $CsPbBr_3$ with a direct band gap.[27] Herein, a circulating flow reactor system (Fig. 4a) was designed and adopted to carry out the activity evaluation of photocatalytic CH_4 oxidation with air as an oxidant. It is worth noting that the flow system can well separate the oxidation products to avoid further oxidation.[41] and the gas–solid system is able to make the catalyst come into full contact with the reaction substrate to avert low solubility of CH_4 under atmospheric pressure. All the photocatalytic experiments were conducted at room temperature under atmospheric pressure. Under the irradiation of a Xe-lamp with a light intensity of 100 mW cm^{-2}, pristine $BiVO_4$ exhibits mediocre photocatalytic activity for CH_4 oxidation, although peroxidation is effectively suppressed in this flow reaction system with a high selectivity of oxygenated hydrocarbons (88.25%). After 3 h of irradiation, the yields of oxygenated hydrocarbon products CH_3OH and HCHO for $BiVO_4$ are only 48.2 and 12.1 μmol g^{-1} h^{-1} (Fig. 4b), respectively, which should be ascribed to its low E_{CB} and short lifetimes of photogenerated carriers. It is noted that individual $CsPbBr_3$ does not have CH_4 oxidation activity, owing to the weak oxidation ability of photogenerated holes in its VB. Nevertheless, loading $CsPbBr_3$ on $BiVO_4$ can bring forth a dramatically improved performance for photocatalytic CH_4 oxidation under the same conditions, exhibiting a volcanic trend with an increase in the $CsPbBr_3$ loading amount (Fig. S13a†). The highest yield of primary products (CH_3OH and HCHO) reached 265.2 μmol g^{-1} h^{-1} (Fig. 4b) over the $CsPbBr_3/BiVO_4$ composite with a mass ratio of 1.5 : 1 between $CsPbBr_3$ and $BiVO_4$, almost 4.4 times that of pristine $BiVO_4$.

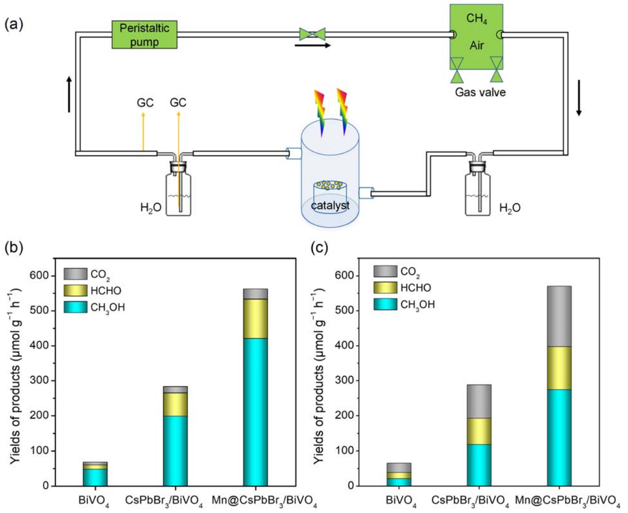

Fig. 4 (a) Schematic diagram of a circulating flow reactor system. (b) Yields of products in the circulating flow system. (c) Yields of products under static conditions: 10 mg photocatalyst, 500 μL water, mixture of CH_4 and air (gas ratio CH_4/air: 10/1), 3 h of 300 W Xe lamp ($\lambda \geq 400$ nm) irradiation at room temperature with a light intensity of 100 mW cm^{-2}.

Moreover, decorating $BiVO_4$ with Mn-doped $CsPbBr_3$ can further promote the photocatalytic conversion of CH_4 as shown in Fig. S13b.† Mn^{2+} ions are considered to act as electron acceptors, which can enhance the separation efficiency of photogenerated carriers in $CsPbBr_3$[39] and thus promote CH_4 conversion. Along with Mn^{2+} content increasing to 0.27 wt%, the primary products (CH_3OH and HCHO) achieved the highest yield of 533.5 μmol g^{-1} h^{-1} (Fig. 4b and S14†) with a high selectivity of 94.84%, which is much higher than those of previously reported photocatalysts under similar mild conditions (Table S2†). Further increasing the proportion of Mn^{2+} results in decreased activity of CH_4 oxidation as commonly observed in photocatalysts with metal doping,[36,42,43] which should be ascribed to the accelerated recombination of carriers induced by the formation of deep trap states in high concentration doping systems. Moreover, repeated experiments were carried out to further evaluate the stability of Mn@$CsPbBr_3$/$BiVO_4$ in the circulating flow system, and the catalysts were dried at 60 °C under vacuum to evaporate all absorbed reactants and products between each run. As shown in Fig. S15,† the catalyst presented just a slight decrease in methanol yield after three runs, indicating the relative stability of inorganic $CsPbBr_3$ in the gas–solid reaction system containing water vapor as commonly demonstrated in photocatalytic CO_2 reduction systems.[44,45] In addition, the XRD patterns of Mn@$CsPbBr_3$/$BiVO_4$ before and after the photocatalytic reaction are similar (Fig. S16†) with only a slight weakening of the characteristic diffraction peak of $CsPbBr_3$ after the photocatalytic reaction. Moreover, the photocatalytic activities of all as-prepared samples for CH_4 oxidation were also assessed under the same conditions except for the gas flow. As illustrated in Fig. 4c, all the samples display evident peroxidation of CH_4 conversion to CO_2 under static conditions with respect to those in the flow reaction system, resulting in noticeably decreased yield and selectivity of oxygenated hydrocarbon products, which demonstrates the unique advantage of the circulating flow system in inhibiting product peroxidation. Regardless, $CsPbBr_3$/$BiVO_4$ still exhibits dramatically enhanced productions of oxygenates (192.4 μmol g^{-1} h^{-1}) relative to that (39.1 μmol g^{-1} h^{-1}) of sole $BiVO_4$ under static conditions, which can be further boosted to 397.5 μmol g^{-1} h^{-1} after incorporating Mn^{2+}, owing to the strong redox capability of the $CsPbBr_3$/$BiVO_4$ heterojunction and its efficient separation of photogenerated carriers.

3.5 Photocatalytic mechanism of CH_4 oxidation

It is well known that photogenerated holes and $^{\bullet}OH$ radicals are both species with highly oxidizing activity and have the potential to oxidize CH_4.[5,46] In order to explore the reaction mechanism of photocatalytic CH_4 oxidation, we first looked into the influence of the water content on the oxidation production of CH_3OH with Mn@$CsPbBr_3$/$BiVO_4$ as the photocatalyst. As presented in Fig. 5a, oxidation products can be ignored in the absence of H_2O, and the yield of CH_3OH increases significantly with an increase in the water amount, indicating that CH_4 may be activated by $^{\bullet}OH$ radicals generated from water oxidation. It is noted that the yield of CH_3OH decreases when the water content is too high, which should be attributed to the instability

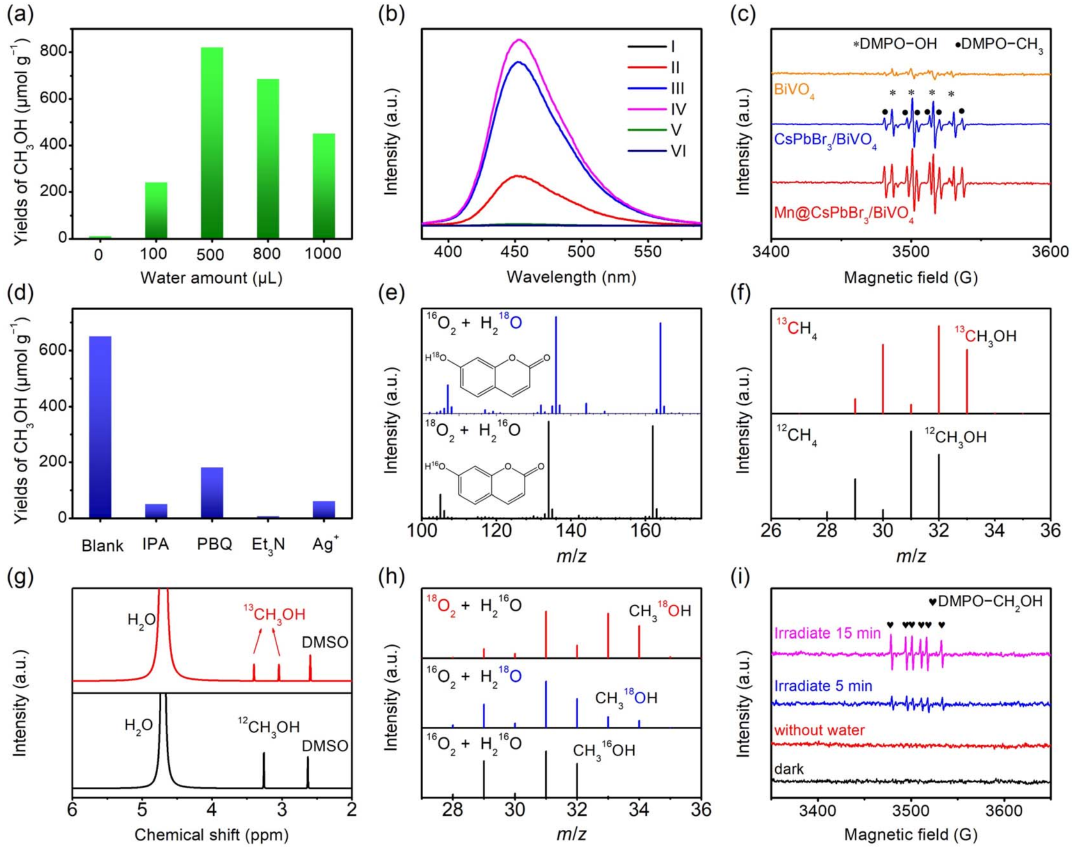

Fig. 5 (a) Yields of CH_3OH by varying the water amount. (b) Fluorescence spectra of coumarin solution taking Mn@$CsPbBr_3$/$BiVO_4$ as the photocatalyst. Line I: without H_2O; line II: without O_2; line III: with H_2O and O_2; line IV: 3 mg $AgNO_3$ instead of O_2; line V: with 10 μL Et_3N; line VI: dark. (c) Comparison of EPR intensities of DMPO–OH and DMPO–CH_3 for various photocatalysts. (d) Yields of CH_3OH with Mn@$CsPbBr_3$/$BiVO_4$ as the photocatalyst under different quenchers. (e) Mass spectra of 7-OH-coumarin generated over Mn@$CsPbBr_3$/$BiVO_4$ with $^{18}O_2$ + $H_2{}^{16}O$ or $^{16}O_2$ + $H_2{}^{18}O$ as feedstocks. (f) Mass spectra of CH_3OH generated over Mn@$CsPbBr_3$/$BiVO_4$ from $^{13}CH_4$ (top) and $^{12}CH_4$ oxidation (below). (g) ^1H NMR spectra of the products produced from $^{13}CH_4$ (top) and $^{12}CH_4$ (below) oxidation. (h) Mass spectra of CH_3OH generated over Mn@$CsPbBr_3$/$BiVO_4$ with $^{18}O_2$ + $H_2{}^{16}O$, $^{16}O_2$ + $H_2{}^{18}O$ or $^{16}O_2$ + $H_2{}^{16}O$ as feedstocks. (i) EPR spectra of DMPO–CH_2OH for photocatalytic CH_3OH oxidation with Mn@$CsPbBr_3$/$BiVO_4$ as the photocatalyst.

of $CsPbBr_3$ in reaction systems containing a large amount of water.[47] Coumarin was employed as a molecular probe to further analyze the $^{\bullet}OH$ production in the photocatalytic system, because coumarin can easily react with the $^{\bullet}OH$ radical to produce 7-OH-coumarin (Fig. S17†), which has high fluorescence with a characteristic peak at 453 nm, and the signal intensity is positively correlated with the concentration of the $^{\bullet}OH$ radical.[48]

There is no PL signal that can be observed without H_2O (Fig. 5b line I), while adding water can bring forth a strong PL signal (Fig. 5b line II), and the PL intensities in different photocatalyst systems show a proportional relationship with photocatalytic performance (Fig. S18†), demonstrating the formation of the $^{\bullet}OH$ radicals in the presence of water. In addition, the PL intensity increases 3-fold along with the introduction of O_2 (Fig. 5b, line III), because O_2 can extract the photogenerated electrons of the photocatalyst and thus promote charge separation. The replacement of O_2 with Ag^+ as an electron scavenger doesn't result in a decrease in PL intensity (Fig. 5b, line IV), suggesting that the $^{\bullet}OH$ radical in the photocatalytic system comes from H_2O oxidation rather than O_2 reduction. This inference can be demonstrated by adding triethylamine (Et_3N) to annihilate the photogenerated holes of the photocatalyst (Fig. 5b, line V) or a background experiment without light irradiation (Fig. 5b, line VI), both of which lead to the disappearance of the PL signal.

The generation of $^{\bullet}OH$ radicals in the photocatalytic system can be further identified by EPR measurements with DMPO as a free radical trapping agent. As presented in Fig. S19,† all photocatalysts with CH_4 activation capability present the typical 1 : 2 : 2 : 1 quartet signal in the absence of CH_4, which can be indexed as the DMPO–OH adducts.[49] Note that the signal intensity of DMPO–OH is positively correlated with the photocatalytic performance, suggesting the critical role of $^{\bullet}OH$ radicals in CH_4 activation. After introducing CH_4 into the system, both the signals corresponding to DMPO–OH and DMPO–CH_3 can be clearly observed in various photocatalysts (Fig. 5c).[50] Moreover, the signal intensity of DMPO–CH_3 is dependent on that of DMPO–OH, implying that the $^{\bullet}CH_3$ intermediates are generated through H abstraction of CH_4 by $^{\bullet}OH$ radicals. The critical role of $^{\bullet}OH$ radicals from H_2O oxidation in the CH_4 activation can also be demonstrated by conducting the controlled experiments. As shown in Fig. 5d, employing isopropyl alcohol (IPA) to annihilate the $^{\bullet}OH$ radical can bring forth a significantly dropped yield of CH_3OH. Moreover, almost no CH_3OH could be detected when photogenerated holes were eliminated by Et_3N (Fig. 5d), revealing that $^{\bullet}OH$ radicals from H_2O oxidation are triggered by the photogenerated holes of the catalyst. The origin of $^{\bullet}OH$ radicals can be further confirmed by isotope labeling experiments. As presented in Fig. 5e, the major mass spectrum signal of 7-^{18}OH-coumarin ($m/z = 164$) can be clearly identified with $^{16}O_2$ and $H_2{}^{18}O$ as feedstocks, while only 7-^{16}OH-coumarin ($m/z = 162$) can be observed in the case of $^{18}O_2$ and $H_2{}^{16}O$, demonstrating that $^{\bullet}OH$ radicals indeed come from water oxidation rather than the photoreduction of O_2.

The role of O_2 in the photocatalytic CH_4 oxidation of the as-prepared Z-scheme heterojunctions was scrutinized by the EPR measurements to monitor the O_2 reduction intermediate. As displayed in Fig. S20,† there are distinct typical signals of DMPO–$O_2{}^-$ after light irradiation for both the $CsPbBr_3/BiVO_4$ and Mn@$CsPbBr_3/BiVO_4$ heterojunctions, revealing that O_2 is reduced to $^{\bullet}O_2{}^-$ by the photogenerated electrons. Mn@$CsPbBr_3/BiVO_4$ exhibits an obviously enhanced DMPO–$O_2{}^-$ signal relative to $CsPbBr_3/BiVO_4$, because Mn^{2+} doping can improve the charge separation efficiency. It is known that $^{\bullet}O_2{}^-$ can be protonated by water to form a $^{\bullet}OOH$ radical, which can be coupled to the $^{\bullet}CH_3$ radical to produce CH_3OOH. Nuclear magnetic resonance (NMR) measurement can confirm the generation of the CH_3OOH intermediate, where a slight peak at 3.76 ppm corresponding to CH_3OOH can be found in the ^1H NMR spectrum (Fig. S21†). Since CH_3OOH is easily reduced to CH_3OH at high photogenerated electron density,[51] it is difficult to detect under the reaction conditions of this work.

Isotope labeling and NMR experiments were further carried out to investigate the carbon source of the oxidation product CH_3OH. As shown in Fig. 5f, in contrast to the mass spectrum of the oxidation product with $^{12}CH_4$ as the feedstock showing the characteristic peaks for $^{12}CH_3OH$ ($m/z = 32$) and corresponding deprotonated fragments, $^{13}CH_3OH$ ($m/z = 33$) and its deprotonated fragment peaks can be clearly identified in the mass spectrum of the oxidation product by employing $^{13}CH_4$ instead of $^{12}CH_4$, demonstrating that the CH_3OH product originates from the CH_4 oxidation. Moreover, there are distinct splitting peaks at 3.04 ppm and 3.40 ppm belonging to $^{13}CH_3OH$ in the ^1H NMR spectrum (top in Fig. 5g) of the oxidation product with $^{13}CH_4$ as the feedstock,[52] and the $^{12}CH_3OH$ signal ($\delta = 3.26$ ppm, below in Fig. 5g) as observed in the case of $^{12}CH_4$ can be detected, further providing clear evidence of CH_4 as the sole carbon source of CH_3OH. In addition, the oxygen source of CH_3OH can be determined by the $^{18}O_2$ and $H_2{}^{18}O$ isotope labeling experiments. As can be seen from the mass spectrum in Fig. 5h (below), only $CH_3{}^{16}OH$ ($m/z = 32$) is produced when $^{16}O_2$ and $H_2{}^{16}O$ are used as feedstocks, while the generation of $CH_3{}^{18}OH$ ($m/z = 34$) can be observed when $H_2{}^{16}O$ is replaced by $H_2{}^{18}O$ (middle in Fig. 5h). Furthermore, employing $^{18}O_2$ instead of $^{16}O_2$ can bring forth a noticeably enhanced signal for $CH_3{}^{18}OH$ (top in Fig. 5h) with respect to the system with $^{16}O_2$ and $H_2{}^{18}O$. These results mean that both O_2 and H_2O are oxygen sources of the CH_3OH product and O_2 is the main contributor, which can be further confirmed by controlled experiments. As presented in Fig. 5d, when the $^{\bullet}O_2{}^-$ radical is annihilated by benzoquinone (PBQ) or photogenerated electrons are extracted by Ag^+ ions, a small amount of CH_3OH is still produced, indicating that the oxygen source of the CH_3OH product is partly from H_2O by the direct coupling of $^{\bullet}OH$ radicals with $^{\bullet}CH_3$ radicals.

It is noted that the signal of DMPO–$O_2{}^-$ for individual $BiVO_4$ cannot be observed after light irradiation (Fig. S20†), indicating that the pathway of O_2 reduction in $BiVO_4$ is different from those in the heterojunctions of $CsPbBr_3/BiVO_4$ and Mn@$CsPbBr_3/BiVO_4$. This difference should be attributed to the inability of the electrons in the CB of $BiVO_4$ ($E_{CB} = 0.50$ V *vs.* SHE) to drive the one-electron reduction of O_2 to $^{\bullet}O_2{}^-$ ($O_2 + e^- \rightarrow {}^{\bullet}O_2{}^-$, 0.08 V *vs.* SHE). For $BiVO_4$, the photogenerated electron should trigger the proton-assistance two-electron reduction reaction of O_2 to H_2O_2 ($O_2 + 2e^- + 2H^+ \rightarrow H_2O_2$, 1.09 V *vs.* SHE),[53] and the H_2O_2 product can be clearly identified in the reaction systems with O_2 participation (Table S3,† entry 1) by liquid chromatography measurements. However, H_2O_2 cannot be detected in the reaction system with $CsPbBr_3$, $CsPbBr_3/BiVO_4$ or Mn@$CsPbBr_3/BiVO_4$ as the photocatalyst (Table S3,† entry 2–4). These results prove again that the photogenerated carrier transfer of the $CsPbBr_3/BiVO_4$ heterojunction is consistent with a direct Z-scheme transfer pathway. Considering that the competitive reaction to produce O_2 ($H_2O_2 + 2h^+ \rightarrow O_2 + 2H^+$) always occurs together with the homolytic cleavage of H_2O_2 to produce $^{\bullet}OH$, resulting in the waste of photogenerated holes,[54] control experiments were further implemented to explore the effect of H_2O_2 on the yield of CH_3OH by photocatalytic CH_4 oxidation with $BiVO_4$. The results show that the introduction of yield levels of H_2O_2 makes no contribution to the yield of CH_3OH and causes a slight inhibition along with an increase in the amount (Fig. S22†), the latter of which should be attributed to the oxidation of H_2O_2 instead of H_2O (Fig. S23†). Moreover, the pathway of CH_3OH production by photocatalytic oxidation of CH_4 with $BiVO_4$ was explored by isotope labeling experiments, as illustrated in Fig. S24† (below). Apparently, only $CH_3{}^{18}OH$ ($m/z = 34$) is produced when $H_2{}^{18}O$ and $^{16}O_2$ are used as feedstocks, while only the generation of $CH_3{}^{16}OH$ ($m/z = 32$) can be observed in the system containing $H_2{}^{16}O$ and $^{18}O_2$ (top in Fig. S24†), implying that the oxygen source of CH_3OH generated by photocatalytic oxidation of CH_4 with $BiVO_4$ almost exclusively comes from H_2O, through the direct coupling of $^{\bullet}OH$ radicals with $^{\bullet}CH_3$ radicals.

The oxidation product CH_3OH can be easily further oxidized to HCHO by the photogenerated holes or $^{\bullet}OH$ radicals, owing to weak thermodynamic constraints.[55] The detailed oxidation mechanism of CH_3OH was further scrutinized in terms of EPR measurements with Mn@$CsPbBr_3/BiVO_4$ as the photocatalyst. As illustrated in Fig. 5i, no signal of hydroxymethyl (DMPO–CH_2OH) or methoxy (DMPO–OCH_3) radicals emerges under dark or anhydrous conditions. In the presence of water, the DMPO–CH_2OH signal[56] can be clearly observed with the extension of light time, indicating that HCHO is mainly derived from H-abstraction of CH_3OH by the $^{\bullet}OH$ radical. The dominant role of $^{\bullet}OH$ radicals from water in the continuous oxidation of CH_3OH can also be demonstrated by the isotope labeling experiments. As shown in Fig. S25,† when $^{18}O_2$ is used to replace $^{16}O_2$, the main overoxidation product is $C^{16}O^{16}O$ ($m/z = 44$), while $C^{18}O^{18}O$ ($m/z = 48$) is the dominant overoxidation product when $H_2{}^{18}O$ is employed instead of $H_2{}^{16}O$. Considering that the oxygen source of CH_3OH is mainly O_2, the results of the above mass spectrum analysis revealed that the continuous oxidation of CH_3OH should undergo H-abstraction by $^{\bullet}OH$ radicals, followed by coupling with $^{\bullet}OH$ radicals and then dehydration to generate deep oxidation products.

Based on the above analysis, we can propose the CH_4 oxidation mechanism of the as-prepared Z-scheme heterojunction Mn@$CsPbBr_3/BiVO_4$ and single $BiVO_4$ photocatalysts respectively as illustrated in Fig. 6. Upon light irradiation, electron–hole pairs are generated in both $CsPbBr_3$ and $BiVO_4$. Thereafter, the photogenerated carriers in the heterojunction achieve charge separation through a Z-scheme pathway (Fig. 6I). The maintained photogenerated holes in the VB of $BiVO_4$ transfer to the surface of $BiVO_4$ and oxidize H_2O to generate $^{\bullet}OH$ radicals and H^+. The C–H bonds of CH_4 are activated through H-abstraction by $^{\bullet}OH$ radicals to form $^{\bullet}CH_3$ intermediates. The obtained $^{\bullet}CH_3$ radicals can be directly coupled with $^{\bullet}OH$ radicals to generate CH_3OH. Meanwhile, the retained photogenerated electrons in the CB of $CsPbBr_3$ transfer to cocatalyst Mn^{2+}, which then induces the one-electron reduction of O_2 to $^{\bullet}O_2{}^-$. The $^{\bullet}O_2{}^-$ radicals can combine with $^{\bullet}CH_3$ radicals and

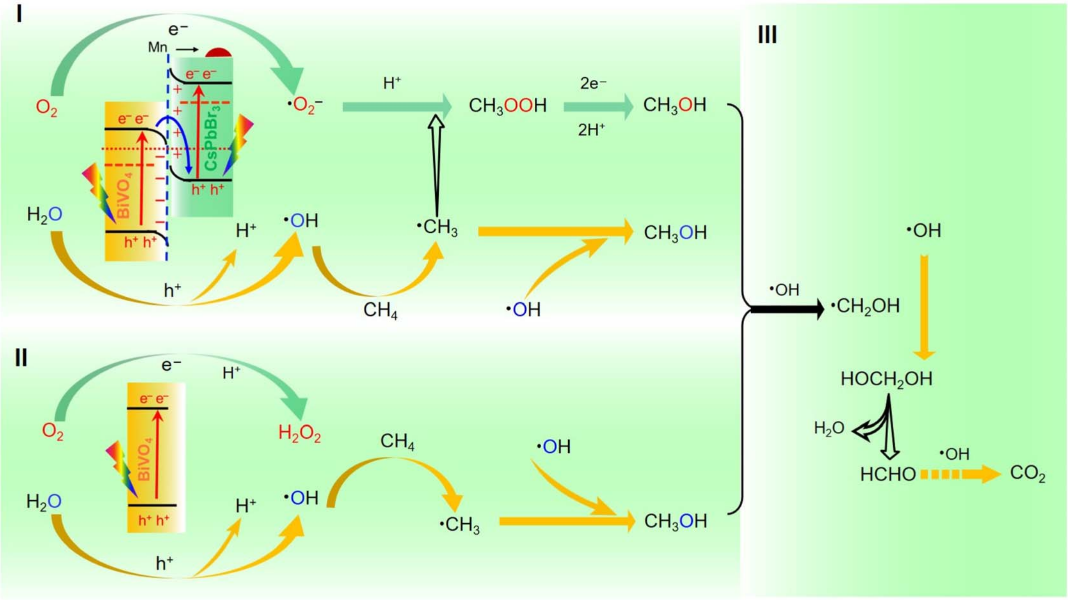

Fig. 6 Schematic diagram of the proposed reaction pathway for CH_4 conversion with Mn@$CsPbBr_3/BiVO_4$ as the photocatalyst.

protons to form CH_3OOH intermediates, which will be swiftly reduced by photogenerated electrons to produce CH_3OH. For individual $BiVO_4$, the photogenerated electrons in the CB selectively trigger proton-assistance two-electron reduction of O_2 to H_2O_2, and the photogenerated holes in the VB oxidize H_2O to generate $^{\bullet}OH$ radicals, which can abstract the H atom of CH_4 to form a $^{\bullet}CH_3$ radical. Then the $^{\bullet}CH_3$ intermediate couples directly with the $^{\bullet}OH$ radical to generate CH_3OH (Fig. 6II). A portion of the as-formed CH_3OH will be further oxidized to HCHO with the assistance of $^{\bullet}OH$ radicals (Fig. 6III). The strong reduction capacity and efficient photogenerated carrier separation account for the significantly enhanced CH_4 photooxidation activity of the Mn@$CsPbBr_3$/$BiVO_4$ photocatalyst with respect to its $BiVO_4$ counterpart.

4 Conclusions

In summary, a halide-perovskite-based photocatalyst Mn@$CsPbBr_3$/$BiVO_4$ with a Z-scheme heterostructure has been successfully constructed through a facile *in situ* growth method, with efforts to achieve efficient photocatalytic CH_4 oxidation under mild conditions. As an example, halide perovskite $CsPbBr_3$ nanocrystals with excellent photophysical properties were first applied in the construction of a photocatalyst for CH_4 conversion, which can significantly boost the photogenerated carrier separation efficiency and reducing ability of the photocatalyst by forming a Z-scheme heterojunction with typical CH_4 oxidation catalyst $BiVO_4$, as confirmed by *in situ* XPS, EPR and photophysical measurements. At room temperature and under atmospheric pressure with air as an oxidant, the total yield of oxygenate products (CH_3OH and HCHO) of the Mn@$CsPbBr_3$/$BiVO_4$ heterojunction reaches up to 533.5 μmol g^{-1} h^{-1} with a high selectivity of 94.8%, which is much superior to those of previously explored photocatalysts under similar mild conditions. Moreover, fluorescence probe and isotope tracing as well as EPR free radical experiments revealed that the oxidation of H_2O by photogenerated holes is the only source of $^{\bullet}OH$, and $^{\bullet}OH$ is the critical active species for activation of CH_4 into a $^{\bullet}CH_3$ intermediate. In addition to O_2, a small part of the oxygen source of oxygenate products comes from H_2O by direct coupling between $^{\bullet}OH$ and $^{\bullet}CH_3$ radicals. Both the reduction and oxidation reaction mechanisms of the Z-scheme photocatalyst for CH_4 conversion have been disclosed in detail, which provides some important clues for the rational design and development of high-performance catalysts for CH_4 photooxidation *via* cost-effective routes.

Conflicts of interest

There are no conflicts to declare.

Acknowledgements

This work was financially supported by the National Key R&D Program of China (2017YFA0700104 and 2022YFA1502902), the Natural Science Foundation of Tianjin City (17JCJQJC43800), NSFC (U21A20286, 21931007 and 21790052), the 111 Project of China, and the Tianjin Research Innovation Project for Postgraduate Students (2021YJSB247).

References

1 S. E. M. Fletcher and H. Schaefer, *Science*, 2019, **364**, 932–933.
2 Q. Bi, M. Wang, M. S. Riaz, X. Du, G. Li and F. Huang, *J. Mater. Chem. A*, 2022, **10**, 23854–23862.
3 X. Meng, X. Cui, N. P. Rajan, L. Yu, D. Deng and X. Bao, *Chem*, 2019, **5**, 2296–2325.
4 H. Song, X. Meng, Z. Wang, H. Liu and J. Ye, *Joule*, 2019, **3**, 1606–1636.
5 X. Li, C. Wang and J. Tang, *Nat. Rev. Mater.*, 2022, **7**, 617–632.
6 V. L. Sushkevich, D. Palagin, M. Ranocchiari and J. A. V. Bokhoven, *Science*, 2017, **356**, 523–527.
7 P. Schwach, X. Pan and X. Bao, *Chem. Rev.*, 2017, **117**, 8497–8520.
8 N. J. Gunsalus, A. Koppaka, S. H. Park, S. M. Bischof, B. G. Hashiguchi and R. A. Periana, *Chem. Rev.*, 2017, **117**, 8521–8573.
9 P. Tang, Q. Zhu, Z. Wu and D. Ma, *Energy Environ. Sci.*, 2014, **7**, 2580–2591.
10 W. Jiang, J. Low, K. Mao, D. Duan, S. Chen, W. Liu, C.-W. Pao, J. Ma, S. Sang, C. Shu, X. Zhan, Z. Qi, H. Zhang, Z. Liu, X. Wu, R. Long, L. Song and Y. Xiong, *J. Am. Chem. Soc.*, 2020, **143**, 269–278.
11 X. Li, J. Xie, H. Rao, C. Wang and J. Tang, *Angew. Chem., Int. Ed.*, 2020, **59**, 19702–19707.
12 Q. Li, Y. Ouyang, H. Li, L. Wang and J. Zeng, *Angew. Chem., Int. Ed.*, 2022, **61**, e202108069.
13 L. K. Dhandole, S. H. Kim and G.-H. Moon, *J. Mater. Chem. A*, 2022, **10**, 19107–19128.
14 J. Xie, R. Jin, A. Li, Y. Bi, Q. Ruan, Y. Deng, Y. Zhang, S. Yao, G. Sankar and D. Ma, *Nat. Catal.*, 2018, **1**, 889–896.
15 X. Yu, V. L. Zholobenko, S. Moldovan, D. Hu, D. Wu, V. V. Ordomsky and A. Y. Khodakov, *Nat. Energy*, 2020, **5**, 511–519.
16 L. Luo, Z. Gong, Y. Xu, J. Ma, H. Liu, J. Xing and J. Tang, *J. Am. Chem. Soc.*, 2022, **144**, 740–750.
17 H. Song, X. Meng, S. Wang, W. Zhou, X. Wang, T. Kako and J. Ye, *J. Am. Chem. Soc.*, 2019, **141**, 20507–20515.
18 X. Chen, Y. Li, X. Pan, D. Cortie, X. Huang and Z. Yi, *Nat. Commun.*, 2016, **7**, 12273.
19 F. Pan, X. Xiang, Z. Du, E. Sarnello, T. Li and Y. Li, *Appl. Catal., B*, 2020, **260**, 118189.
20 H. Tang, T. Ju, Y. Dai, M. Wang, Y. Ma, M. Wang and G. Zheng, *J. Mater. Chem. A*, 2022, **10**, 18978–18988.
21 Y. Fan, W. Zhou, X. Qiu, H. Li, Y. Jiang, Z. Sun, D. Han, L. Niu and Z. Tang, *Nat. Sustain.*, 2021, **4**, 509–515.
22 Y. Zhou, L. Zhang and W. Wang, *Nat. Commun.*, 2019, **10**, 506.
23 P. Xie, J. Ding, Z. Yao, T. Pu, P. Zhang, Z. Huang, C. Wang, J. Zhang, N. Zecher-Freeman, H. Zong, D. Yuan, S. Deng, R. Shahbazian-Yassar and C. Wang, *Nat. Commun.*, 2022, **13**, 1375.

24 L. Luo, L. Fu, H. Liu, Y. Xu, J. Xing, C.-R. Chang, D.-Y. Yang and J. Tang, *Nat. Commun.*, 2022, **13**, 2930.

25 K. Zheng, Y. Wu, J. Zhu, L. Li, S. Wang, M. Fan, J. Hu, W. Yan, J. Zhu, Y. Sun and Y. Xie, *J. Am. Chem. Soc.*, 2022, **144**, 12357–12366.

26 S. Song, H. Song, L. Li, S. Wang, W. Chu, K. Peng, X. Meng, Q. Wang, B. Deng, Q. Liu, Z. Wang, Y. Weng, H. Hu, T. Kako and J. Ye, *Nat. Catal.*, 2021, **4**, 1032–1042.

27 M. S. A. S. Shah, C. Oh, H. Park, Y. J. Hwang, M. Ma and J. H. Park, *Adv. Sci.*, 2020, **7**, 2001946.

28 Q. A. Akkerman, G. Rainò, M. V. Kovalenko and L. Manna, *Nat. Mater.*, 2018, **17**, 397–405.

29 J. Low, J. Yu, M. Jaroniec, S. Wageh and A. A. Al-Ghamdi, *Adv. Mater.*, 2017, **29**, 1601694.

30 Q. Xu, L. Zhang, J. Yu, S. Wageh, A. A. Al-Ghamdi and M. Jaroniec, *Mater. Today*, 2020, **21**, 1042–1063.

31 S. Shyamal, S. K. Dutta, T. Das, S. Sen and S. Chakraborty, *J. Phys. Chem. Lett.*, 2020, **11**, 3608–3614.

32 S. Murcia-Lopez, K. Villa, T. Andreu and J. R. Morante, *ACS Catal.*, 2014, **4**, 3013–3019.

33 B. Dai, G. M. Biesold, M. Zhang, H. Zou, Y. Ding, Z. L. Wang and Z. Lin, *Chem. Soc. Rev.*, 2021, **50**, 13646–13691.

34 B. Dai, J. Guo, C. Gao, H. Yin, Y. Xie and Z. Lin, *Adv. Mater.*, 2023, 2210914.

35 D. Lee, W. Wang, C. Zhou, X. Tong, M. Liu, G. Galli and K.-S. Choi, *Nat. Energy*, 2021, **6**, 287–294.

36 J. Cheng, Y. Mu, L. Wu, Z. Liu, K. Su, G. Dong, M. Zhang and T. Lu, *Nano Res.*, 2022, **15**, 1845–1852.

37 J. Low, B. Dai, T. Tong, C. Jiang and J. Yu, *Adv. Mater.*, 2019, **31**, 1802981.

38 W. Zhang, A. R. Mohamed and W.-J. Ong, *Angew. Chem., Int. Ed.*, 2020, **59**, 22894–22915.

39 L. Wu, Y. Wang, M. Kurashvili, A. Dey, M. Cao, M. Doeblinger, Q. Zhang, J. Feldmann, H. Huang and T. Debnath, *Angew. Chem., Int. Ed.*, 2022, **61**, e202115852.

40 F. Zhong, Y. He, Y. Sun, F. Dong and J. Sheng, *J. Mater. Chem. A*, 2022, **10**, 22915–22928.

41 B. An, Z. Li, Z. Wang, X. Zeng, X. Han, Y. Cheng, A. M. Sheveleva, Z. Zhang, F. Tuna, E. J. L. McInnes, M. D. Frogley, A. J. Ramirez-Cuesta, L. S. Natrajan, C. Wang, W. Lin, S. Yang and M. Schröder, *Nat. Mater.*, 2022, **21**, 932–938.

42 J. Wang, T. Xia, L. Wang, X. Zheng, Z. Qi, C. Gao, J. Zhu, Z. Li, H. Xu and Y. Xiong, *Angew. Chem., Int. Ed.*, 2018, **57**, 16447–16451.

43 Z. Zhang, Q. Wu, G. Johnson, Y. Ye, X. Li, N. Li, M. Cui, J. D. Lee, C. Liu, S. Zhao, S. Li, A. Orlov, C. B. Murray, X. Zhang, T. B. Gunnoe, D. Su and S. Zhang, *J. Am. Chem. Soc.*, 2019, **141**, 16548–16552.

44 Y. Jiang, J.-F. Liao, H.-Y. Chen, H.-H. Zhang, J.-Y. Li, X.-D. Wang and D.-B. Kuang, *Chem*, 2020, **6**, 766–780.

45 R. Cheng, Z.-B. Liang, L. Zhu, H. Li, Y. Zhang, C.-F. Wang and S. Chen, *Angew. Chem., Int. Ed.*, 2022, **61**, e202204371.

46 Y. Jiang, Y. Fan, S. Li and Z. Tang, *CCS Chem.*, 2023, **5**, 30–54.

47 Y. Wei, Z. Cheng and J. Lin, *Chem. Soc. Rev.*, 2019, **48**, 301–350.

48 Q. Xiang, J. Yu and P. K. Wong, *J. Colloid Interface Sci.*, 2011, **357**, 163–167.

49 Y. Li, S. Ouyang, H. Xu, X. Wang, Y. Bi, Y. Zhang and J. Ye, *J. Am. Chem. Soc.*, 2016, **138**, 13289–13297.

50 M. H. Ab Rahim, M. M. Forde, R. L. Jenkins, C. Hammond, Q. He, N. Dimitratos, J. A. Lopez-Sanchez, A. F. Carley, S. H. Taylor, D. J. Willock, D. M. Murphy, C. J. Kiely and G. J. Hutchings, *Angew. Chem., Int. Ed.*, 2013, **52**, 1280–1284.

51 M. A. Bañares, L. J. Alemany, M. López Granados, M. Faraldos and J. L. G. Fierro, *Catal. Today*, 1997, **33**, 73–83.

52 N. Agarwal, S. J. Freakley, R. U. McVicker, S. M. Althahban, N. Dimitratos, Q. He, D. J. Morgan, R. L. Jenkins, D. J. Willock, S. H. Taylor, C. J. Kiely and G. J. Hutchings, *Science*, 2017, **358**, 223–227.

53 D. Tsukamoto, Y. Shiraishi and T. Hirai, *Catal. Sci. Technol.*, 2013, **3**, 2270–2277.

54 Y. Xing, Z. Yao, W. Li, W. Wu, X. Lu, J. Tian, Z. Li, H. Hu and M. Wu, *Angew. Chem., Int. Ed.*, 2021, **60**, 8889–8895.

55 J. Schneider and D. W. Bahnemann, *J. Phys. Chem. Lett.*, 2013, **4**, 3479–3483.

56 T. Baran, A. Dibenedetto, M. Aresta, K. Kruczała and W. Macyk, *ChemPlusChem*, 2014, **79**, 708–715.